RSC Advances

PAPER

View Article Online
View Journal | View Issue

Cite this: *RSC Adv.*, 2022, **12**, 31518

First-principles investigation of potential water-splitting photocatalysts and photovoltaic materials based on Janus transition-metal dichalcogenide/WSe_2 heterostructures

Samuel Tilahun Ayele,[ab] Kingsley O. Obodo[cd] and Georgies Alene Asres *[a]

Two-dimensional materials have been shown to exhibit exotic properties that make them very interesting for both photo-catalytic and photo-voltaic applications. In this study, van der Waals corrected density functional theory calculations were carried out on heterostructures of MoSSe/WSe_2, WSSe/WSe_2, and WSeTe/WSe_2. The heterostructures are semiconductors with type II band alignments which are advantageous for electron–hole pair separation. The HSE06 level electronic band gap was found to be 1.093 eV, 1.427 eV and 1.603 eV for MoSSe/WSe_2, WSSe/WSe_2, and WSeTe/WSe_2 respectively. We have considered eight high symmetry stacking patterns for each of the heterostructures, and among them the most stable stacking orders were ascertained based on the interlayer binding energies. The binding energies of the most stable MoSSe/WSe_2, WSSe/WSe_2, and WSeTe/WSe_2 heterostructures were found to be −0.0604 eV, −0.1721 eV, and −0.3296 eV with an equilibrium interlayer space of 5.75 Å, 4.05 Å, and 4.76 Å respectively. The Power Conversion Efficiency (PCE) was found to be 20, 19.98, and 18.24 percent for the MoSSe/WSe_2, WSSe/WSe_2, and WSeTe/WSe_2 heterostructures, respectively. The results show that they can serve as suitable photovoltaic materials with high efficiency, thus, opening the possibilities of developing solar cells based on 2D Janus/TMD heterostructures. The most stable heterostructures are also tested for photocatalytic water splitting applications and WSeTe/WSe_2 shows excellent photocatalytic activity by being active for full water splitting at pH = 7 and pH = 14, the MoSSe/WSe_2 heterostructure is good for the oxygen evolution reaction and WSSe/WSe_2 is active for the hydrogen evolution reaction.

Received 8th August 2022
Accepted 26th October 2022

DOI: 10.1039/d2ra04964c

rsc.li/rsc-advances

1 Introduction

Since graphene was isolated from highly oriented pyrolytic graphite (HOPG) for the first time in 2004,[1] graphene's success has stimulated an explosive interest in other 2D materials, where using different elements opens up new possibilities for exciting new physics and ultimately thin devices.[2] To synthesize 2D materials, a variety of chemical and physical methods, such as mechanical exfoliation, chemical exfoliation of bulk structures, chemical vapor deposition (CVD) of thin films, and so on, can be used.[3,4] There are various kinds of two-dimensional (2D) materials.[5–12] Some of the most common 2D materials are transition metal dichalcogenides (TMDs), whose chemical composition is usually represented by MX_2, and whose structure consists of one transition metal (M) atom layer sandwiched between two chalcogen (X) atom layers.[13–15] MX_2 monolayers have a direct band gap between 1.0 and 1.9 eV,[16,17] excellent carrier mobility, and a strong spin–orbit coupling (SOC) effect due to the d orbitals of the heavy metal atom.[18] Among the TMDs of group-VIB, WSe_2 has emerged as a material with many outstanding properties,[19,20] and the first exfoliation occurred in 2013.[21–23] Bulk WSe_2 was used previously in photovoltaic cells[24,25] and for photoelectrochemical (PEC) hydrogen production[26] because of its suitable band gap and long-term stability. Also with layer-by-layer stacking, WSe_2 demonstrates newly explored properties after being encapsulated with atomically thin materials, or incorporated in van der Waals heterostructures.[27–29]

The successful experimental synthesis of the MoSSe compound in 2014 added a new member to the TMD family, which is known as Janus MXY (M = Mo, W; X, Y = S, Se).[30] Due to the different atomic species on each side of the metal layer, they exhibit a high dipole across the plane. The Janus monolayer is composed of three atomic layers stacked in the X–M–Y

[a]*Center for Materials Engineering, Addis Ababa Institute of Technology, Addis Ababa University, School of Multi-disciplinary Engineering, Addis Ababa, 1000, Ethiopia. E-mail: georgies.alene@aait.edu.et; Tel: +251 902639816*

[b]*Space Science and Geospatial Institute, Addis Ababa, Ethiopia*

[c]*HySA Infrastructure Centre of Competence, Faculty of Engineering, North-West University, South Africa (NWU), 2531, South Africa*

[d]*National Institute of Theoretical and Computational Sciences, Johannesburg, 2000, South Africa*

sequence. The spin–orbit coupling and the band structures of the Janus MXY monolayers, like their parent TMD structure, display stable spin splitting at the band margins near the *K* point.[31] When the Janus MXY (JTMD) comes into contact with other materials on different sides, it can form unique structures with a variety of properties.[32] JTMD monolayers have moderate band gaps between 1.37 and 1.96 eV,[33] pronounced visible-light absorption, and a carrier mobility ranging from 28 to 606 $cm^2 V^{-1} s^{-1}$ with type-II band alignment present in most cases. Type-II band alignment forms in JTMD bilayers with significantly large band offset, which is beneficial for exciton lifetimes and thus more appealing in light-energy conversion.[30] This observation makes JTMD monolayers promising candidates for electronics, photovoltaics, and photocatalysis.[34] MoSSe's mirror asymmetry reveals an intrinsic out-of-plane electric field.[35,36] Also, MoSSe has been shown to possess an enhanced Rashba effect and a high exciton binding energy,[37,38] and it is also an excellent photocatalyst for solar water decomposition.[35,39–41] MoSSe's unique properties have opened up new avenues for application.[30] The small effective mass of MoSSe leads to higher carrier mobility, which is highly desirable for high performance device applications.[42] WSSe and WSeTe have higher carrier mobilities due to their small effective masses and large elastic constants. Compared with conventional TMD monolayers such as MoS_2 ($60 \sim 200$ $cm^2 V^{-1} s^{-1}$),[43,44] WSSe and WSeTe exhibit higher carrier mobilities. Recently, Janus TMD structures have been widely investigated, following the growth of a MoSSe monolayer using a synthetic strategy with vertical dipoles.[45] Combining polarized Janus MXY monolayers to form bilayer structures or with other 2D layers to form vdW heterostructures results in new properties.[30]

The weak vdW forces between two different layered materials result in an energetically stable heterostructure.[46,47] The interface of a 2D heterostructure results in various interesting properties, which enhance the electronic, optical, and photocatalytic abilities.[8,48,49] As a result, a variety of 2D heterostructure materials have been developed and used as p–n junctions,[50] photocatalysts,[51] photovoltaic devices, field-effect transistors,[52] biosensors, light emitting diodes, light detectors, and energy storage devices.[53] In this study, first-principles calculations were performed based on DFT to investigate the electronic, photocatalytic, and photovoltaic properties of MoSSe/WSe_2, WSSe/WSe_2, and WSeTe/WSe_2 vdW heterostructures. Eight different heterostructure configurations were considered, and the structures with minimum binding energy were selected for further analysis. The electronic properties of MoSSe–WSe_2, WSSe–WSe_2, and WSeTe–WSe_2 vdW heterostructures were evaluated and we observed that they are all semiconducting. The results show that the vdW heterostructures exhibit type II band alignment, which is an excellent property for efficiently separating excitons, good for photovoltaics and photocatalytic water splitting. The Power Conversion Efficiency (PCE) was found to be 20 percent, 19.98 percent, and 18.24 percent for the MoSSe/WSe_2, WSSe/WSe_2, and WSeTe/WSe_2 heterostructures, respectively, which makes them good candidates for photovoltaic solar cells. WSeTe/WSe_2 shows excellent photocatalytic activity by being active for full water splitting under basic and acidic conditions, the MoSSe/WSe_2 heterostructure is good for the oxygen evolution reaction and WSSe/WSe_2 is active for the hydrogen evolution reaction. In general, we were the first to study these heterostructures, and the systems performed well in photovoltaic and water splitting applications. The heterobilayers presented in this research can then be applied in 2D excitonic solar cells. Based on our findings, these two-dimensional materials will aid in the development and implementation of alternative/renewable energy sources.

2 Computational methods

First principles calculations were performed using Quantum ESPRESSO and CASTEP code,[54] which is based on density functional theory (DFT) with a plane-wave basis set and pseudopotentials method. The description of electron exchange and correlation functionals was addressed using the generalized gradient approximation (GGA) of the Perdew–Burke–Ernzerhof (PBE) functional.[55,56] The hybrid Heyde–Scuseriae–Ernzerhof (HSE06) functional was also used to provide more accurate band gaps for all heterostructures.[57,58] During the optimization and self-consistent calculations, $12 \times 12 \times 1$ *k*-point meshes were used to sample the Brillouin zone. An energy cutoff of 600 Ry and 800 Ry was used. A relatively large vacuum space of 24 Å was employed to eliminate the unphysical interaction between adjacent slabs. All atomic positions were completely relaxed until the force was less than 0.01 eV $Å^{-1}$, and the overall energy convergence criterion was set to 10–5 eV. Grimme's DFT-D2 method has been widely used to provide a reliable description of all types of vdW heterostructures;[59,60] as a result, throughout the calculations, the Grimme DFT-D2 dispersion correction method is used.

3 Results and discussion

3.1 Structural properties and energetics

The crystal structures of the MoSSe, WSSe, WSeTe and WSe_2 monolayers were optimized (Fig. 1), and the calculated lattice constants of MoSSe, WSSe, WSeTe and WSe_2 are 3.26 Å, 3.26 Å, 3.45 Å and 3.34 Å respectively. The bond lengths of Mo–Se, Mo–S, W–Se, W–S and W–Te in the optimized monolayers of MoSSe, WSSe, WSeTe and WSe_2 are 2.54 Å, 2.42 Å, 2.55 Å, 2.42 Å and 2.72 Å, respectively. The calculated lattice constants and bond lengths agree with the values obtained in previous studies.[5,16,42,51,61–63] The calculated lattice mismatch is expressed by[64]

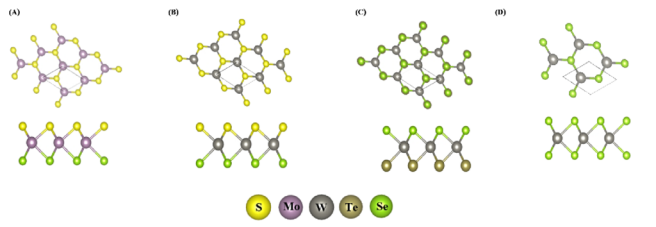

Fig. 1 Top and side views of (A) MoSSe, (B) WSSe, (C) WSeTe, and (D) WSe_2 monolayers.

$$\Delta a/a(\text{substrate}) = [a - a(\text{substrate})/a(\text{substrate})] \times 100 \quad (1)$$

where a(substrate) is the lattice constant of the substrate. When the lattice mismatch is less than 5 percent, the two layers can be experimentally fabricated.[64] The lattice mismatches of MoSSe/WSe_2, WSSe/WSe_2, and WSeTe/WSe_2 are 2.39 percent, 2.39 percent, and 3.19 percent respectively, which are appropriate, and so the formation of these vdW heterostructures is experimentally realizable. Please note that initially we considered six Janus materials and excluded three of them (MoSTe, MoSeTe and WSTe) from our study since they did not have suitable lattice mismatch.

The electronic band structures of the monolayers are calculated using GGA-PBE as shown in Fig. 2. Also, the HSE06 electronic band gaps were determined and applied for the determination of both the photocatalytic and photovoltaic properties. The GGA-PBE (HSE06) electronic band gaps for the MoSSe, WSSe, and WSe_2 monolayers are direct, with values of 2.028 eV, 2.195 eV and 1.967 eV respectively with the conduction band minimum (CBM) and the valence band maximum (VBM) located at the K points, while WSeTe possesses an indirect band gap of 1.775 eV as shown in Fig. 2.

The heterostructures of MoSSe, WSSe and WSeTe with WSe_2 monolayers were constructed as shown in Fig. 3. We considered eight possible highly symmetric stacking patterns for each of the heterostructures and Fig. 3 shows MoSSe/WSe_2 as an example.

The AAI stacking pattern refers to the W transition metal atom of the WSe_2 layer being placed on top of the metal atom of the second layer, as well as the chalcogen of WSe_2 being aligned with the Janus TMD's chalcogen atom. AAI-Se stacking is similar to AAI stacking, however WSe_2 is facing Se rather than S as in AAI stacking. AAII stacking has the transition metal atom from the WSe_2 monolayer on top of the chalcogen atom of the Janus TMD, while the chalcogen atom from WSe_2 is on top of the metal atom of the Janus TMD. AAII-Se stacking is similar to AAII but the Se of the Janus TMD is facing towards WSe_2. ABI stacking refers to the vertical alignment of metal atoms; the W from WSe_2 is on top of the metal atom from the Janus TMD, but the WSe_2 and Janus TMD chalcogen atoms are not vertically aligned. ABI-Se stacking is similar to ABI stacking, except that the Se atoms of the Janus TMD are facing the top WSe_2 layer. ABII stacking is defined as WSe_2 chalcogen atoms on top of Janus TMD metal atoms, but the WSe_2 metal and Janus TMD chalcogen atoms are not vertically aligned. The ABII-Se stacking configuration is similar to ABII but the Se atoms of the Janus structure are facing towards the top WSe_2 layer. The stability of the heterostructures is determined by the binding energy E_b.[65,66] The formula of the binding energy is:

$$E_b = E - E_1 - E_2 \quad (2)$$

where E is the total energy of the heterostructure, E_1 is the energy of the isolated MoSSe/WSeTe/WSSe monolayer and E_2 is the isolated WSe_2 monolayer's energy. The most stable stacking mode for the MoSSe/WSe_2 heterostructure is ABI-Se, while the most stable stacking mode for the WSSe/WSe_2 and WSeTe/WSe_2 heterostructures is AAII-Se. The binding energies of the MoSSe/WSe_2, WSSe/WSe_2, and WSeTe/WSe_2 heterostructures are −0.0604 eV, −0.1721 eV, and −0.3296 eV respectively with an interlayer spacing/distance of 5.75 Å, 4.05 Å and 4.76 Å respectively.

3.2 Electronic structure

The projected electronic band structures of the most stable MoSSe/WSe_2, WSSe/WSe_2, and WSeTe/WSe_2 vdW heterostructures calculated using GGA-PBE are shown in Fig. 4(A)–(C). The projected band structure does not provide sufficient information for identifying the band alignment, for instance in the case of WSeTe/WSe_2, we cannot identify which compound the tungsten is attributed to. Therefore, we have plotted the band edge alignment for the heterostructures in Fig. 5. The band edge alignment shows that MoSSe/WSe_2 and WSeTe/WSe_2 are type-II band alignment semiconductors with a direct band gap of 1.093 eV and 1.603 eV respectively. The CBM and VBM of the MoSSe/WSe_2 and WSeTe/WSe_2 heterostructures are located at the K point in the BZ. The WSSe/WSe_2 heterostructure is also

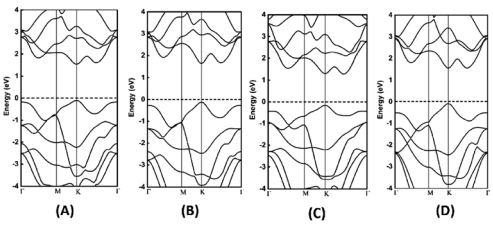

Fig. 2 Electronic GGA-PBE band structures of (A) MoSSe, (B) WSSe, (C) WSeTe, and (D) WSe_2 monolayers.

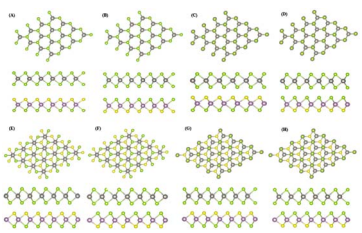

Fig. 3 Top and side view stacking patterns of MoSSe/WSe_2, WSSe/WSe_2, and WSeTe/WSe_2 heterostructures: (A) AAI, (B) AAI-Se, (C) AAII, (D) AAII-Se, (E) ABI, (F) ABI-Se, (G) ABII, and (H) ABII-Se.

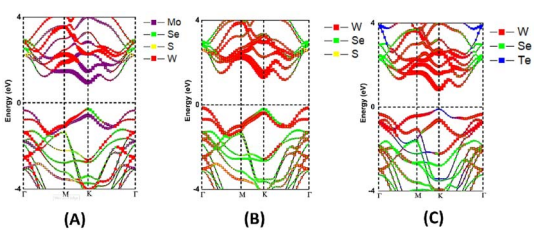

Fig. 4 Band structure of (A) MoSSe/WSe_2, (B) WSSe/WSe_2 and (C) WSeTe/WSe_2 vdW heterostructures. Purple, green, yellow, red, and blue dots represent Mo, Se, S, W, and Te atoms, respectively.

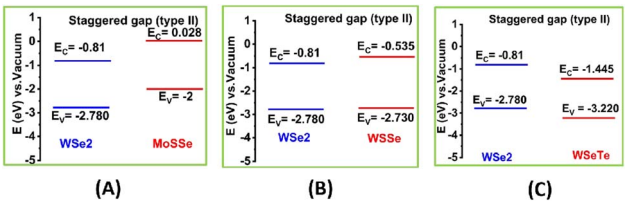

Fig. 5 Type-II band alignment of (A) $MoSSe/WSe_2$, (B) $WSSe/WSe_2$, and (C) $WSeTe/WSe_2$ vdW heterostructures.

a type-II band alignment semiconductor with an indirect band gap of 1.427 eV.

The transfer of photo-excited electrons and holes in type-II vdW heterostructures is advantageous for photo energy detection and harvesting. Photon absorption in a type-II heterostructure generates excited free carriers. In an ultrafast time scale, free carriers split into electrons and holes at the donor and acceptor. During the free carrier dissociation process, the electrodes will generate a photocurrent.[67] The electronic band alignment of the $MoSSe/WSe_2$, $WSSe/WSe_2$, and $WSeTe/WSe_2$ vdW heterostructures is shown in Fig. 5(A), (B) and (C) respectively. They all exhibit type II band alignment which facilitates efficient exciton separation and is good for the intended applications (photovoltaic solar cells and water splitting).

3.3 Photovoltaics

With band gaps in the optical range, the three heterostructures can also be assessed for photovoltaic applications. A standard metric to determine whether a material would be useful for photovoltaic applications is the power conversion efficiency (PCE), or the fraction of incident sunlight that can be converted into electricity. The PCE is defined as[68–70]

$$\frac{\mathrm{FF}\,V_{\mathrm{OC}}J_{\mathrm{sc}}}{P_{\mathrm{sun}}} \tag{3}$$

using

$$eV_{\mathrm{OC}} = E_{\mathrm{g}} - E_{\mathrm{loss}} \tag{4}$$

$$J_{\mathrm{sc}} = \int_{E}^{\infty} \frac{S(E)}{E}\mathrm{d}E \tag{5}$$

$$P_{\mathrm{sun}} = \int_{0}^{\infty} S(E)\mathrm{d}E \tag{6}$$

where V_{OC} is the open circuit voltage, defined as the energy difference per unit charge between the band gap E_{g} and the inherent energy losses E_{loss}, $S(E)$ is the power provided by the sun per unit area and photon energy, E is the photon energy, J_{sc} is the short-circuit current, or the current that can be generated by all photons with energy greater than or equal to the band gap, and FF is the fill factor. $S(E)$ is obtained using the NREL AM1.5 dataset. The fill factor FF and the energy losses E_{loss} are empirical factors and cannot be calculated *via* first principles. A prior experimental study found that a MoS_2/p-Si heterostructure exhibited a fill factor of 0.57.[71] As this is the only experimental paper that the authors are aware of that reports a fill factor for a TMD, we take this to be our fill factor. The smallest E_{loss} that has been reported in the literature is 0.3 eV.[69] We take this as our E_{loss} to set an upper bound on the possible power conversion efficiencies the three heterostructures could exhibit. Using eqn (3) and the HSE06 calculated band gaps for the considered heterostructures, the PCEs are calculated. The calculated PCEs for the heterostructures are 20 percent, 19.98 percent, and 18.24 percent for the $MoSSe/WSe_2$, $WSSe/WSe_2$, and $WSeTe/WSe_2$ heterostructures, respectively. These values are much better than those for the InSe/Te (13.8 percent)[72] vdW heterostructure, WSe_2/WS_2 (2.4 percent)[73] vdW heterostructure, PN/WSe_2 (13.8 percent)[56] vdW heterostructure, type-II GaTe/InSe (9.1 percent)[56] and GaTe/InS (11.52 percent)[56,74] vdW heterostructure which have been recently reported.

3.4 Photocatalytic water splitting

Photocatalytic overall water splitting to form hydrogen and oxygen has received a lot of attention as a potential source of renewable energy[75] that can be used to address global energy and environmental issues. The catalytic water splitting reaction ($H_2O \rightarrow 1/2O_2 + H_2$) is a thermodynamically uphill reaction with a net Gibbs free energy of 237 kJ mol^{-1}.[76,77] Overall water splitting for the production of H_2 using a semiconductor material is similar to the photosynthetic reaction in many ways.[76] In general, the photocatalytic water splitting reaction on semiconductor materials consists of three major steps, which are: (I) absorption of light irradiation with energy greater than the semiconductor band gap generates electron (e^-) and hole (h^+) pairs within the semiconductor material, (II) the generated electrons and holes are separated, and these charges migrate to the semiconductor interface, and (III) surface chemical reactions occur between these carriers and various compounds (*e.g.*, H_2O); electrons and holes produce H_2 and O_2, respectively.[77,78] The preliminary requirement for application of a material in photocatalytic overall water splitting is that the redox reaction on the surface of the photocatalyst occurs when the reduction and oxidation potentials are above and below the CB and VB levels, respectively.[42,58] For overall water splitting, electrons reduce water molecules to generate H_2 and holes oxidize water molecules to form O_2.[79] The band levels of the $MoSSe/WSe_2$, $WSSe/WSe_2$, and $WSeTe/WSe_2$ vdW heterostructures are shown in Fig. 6.

It is important to note that under the operating conditions in an aqueous environment the relative positions of the HER and OER redox potentials to the band edges of the heterostructures

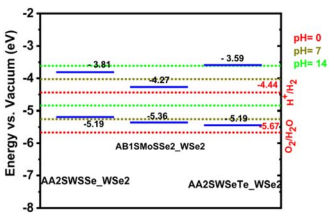

Fig. 6 Band edge alignment to HER and OER redox potentials at varying pH. The redox potentials for the hydrogen evolution reaction and the oxygen evolution reaction at pH = 0, 7, and 14 are indicated in red, olive green, and green, respectively.

will differ from the relative positions of the pH = 0 redox potentials to those of the vacuum band edges of the heterostructures. The HER and OER redox potentials are functions of pH and shift according to the Nernst equation (eqn (7))[80]

$$E(\mathrm{pH}) = E(\mathrm{pH} = 0) + 0.059 \times \mathrm{pH} \quad (7)$$

where all energies in eqn (7) are in eV. We compare the calculated band edges to those of the HER and OER at various pH values. The relative alignment of the band edges of the heterostructures to the HER and OER potentials at pH = 0, 7, and 14 is plotted in Fig. 6. From the figure, we can see that the WSeTe/WSe_2 heterostructure is good for full water splitting at pH 7 and 14 since the band edges straddle the redox potentials of water at these pH values. The same structure is not suitable for full water splitting at pH = 0, however even at this pH value it is good for the hydrogen evolution reaction. The MoSSe/WSe_2 heterostructure is good for the oxygen evolution reaction at pH = 7 and 14 and good for the hydrogen evolution reaction at pH = 0. The WSSe/WSe_2 heterostructure is good for the hydrogen evolution reaction at pH = 0 and pH = 7 and good for the oxygen evolution reaction at pH = 14. In general, the considered heterostructures are good for partial water splitting applications and in particular, the WSeTe/WSe_2 heterostructure is good for full water splitting under basic and acidic conditions.

3.5 Conclusion

In this study, a first principles DFT-based model was used to calculate the electronic properties of MoSSe/WSe_2, WSSe/WSe_2, and WSeTe/WSe_2 vdW heterostructures for solar cell and photocatalytic water splitting applications. Eight different stacking modes were investigated to determine the most stable configuration based on the binding energies. In addition, the optimal interlayer spacing was determined for the considered heterostructures. From the eight stacking configurations considered, three possible vdW heterostructures were obtained as the most stable configurations, which are ABI-Se for MoSSe/WSe_2, AAII-Se for WSSe/WSe_2 and AAII-Se for WSeTe/WSe_2. The MoSSe/WSe_2 and WSeTe/WSe_2 heterostructures are direct band gap materials with band gap values of 1.093 and 1.603 eV respectively, while WSSe/WSe_2 has an indirect band gap of 1.427 eV. The binding energies of the MoSSe/WSe_2, WSSe/WSe_2, and WSeTe/WSe_2 heterostructures are found to be −0.0604 eV, −0.1721 eV, and −0.3296 eV with an interlayer distance of 5.75 Å, 4.05 Å, and 4.76 Å respectively. The obtained PCE value for photovoltaic applications is 20 percent, 19.98 percent, and 18.24 percent for the MoSSe/WSe_2, WSSe/WSe_2, and WSeTe/WSe_2 heterostructures, respectively, which is good and makes the structures promising for this application. In addition, the band edge alignment is type two which assists charge separation, and coupled with the intrinsic polar nature of Janus materials, this strengthens their application for photovoltaics. Regarding the photocatalytic water splitting application we found out that the WSeTe/WSe_2 heterostructure is good for full water splitting under basic and acidic conditions. We also found out that not all of these heterostructures can satisfy the band edge requirements for full water splitting, however they can be applied in the H_2 evolution reaction and oxygen evolution reaction under visible light irradiation. In general, this study reveals that making Janus heterostructures is a good way to tune the electronic properties and engineer materials for photovoltaics and photocatalytic water splitting.

Conflicts of interest

There are no conflicts to declare.

Acknowledgements

This work was substantially sponsored by funding from Addis Ababa University through a thematic project (Grant No. RD/LT-095/2019). We also gratefully acknowledge Dr Tekalign T. Debela, Postdoctoral Associate at the University of Oregon, for providing insight and expertise that considerably aided the research. The authors thank the Centre for High Performance Computing (CHPC) in Cape Town, South Africa, for the computational resources used in this study. Samuel acknowledges the Space Science and Geospatial Institute for financial support, and KOO acknowledges the HySA Infrastructure Centre of Competence, Faculty of Engineering, North-West University for their financial support.

References

1 A. Kuc, T. Heine and A. Kis, *MRS Bull.*, 2015, **40**, 577–584.
2 B. T. Beshir, K. O. Obodo and G. A. Asres, *RSC Adv.*, 2022, **12**, 13749–13755.
3 A. Rawat, R. Ahammed, Dimple, N. Jena, M. K. Mohanta and A. De Sarkar, *J. Phys. Chem. C*, 2019, **123**, 12666–12675.
4 G. A. Asres, A. Dombovari, T. Sipola, R. Puskás, A. Kukovecz, Z. Kónya, A. Popov, J.-F. Lin, G. S. Lorite, M. Mohl, *et al.*, *Sci. Rep.*, 2016, **6**, 1–7.
5 Z. Zhu, K. Ren, H. Shu, Z. Cui, Z. Huang, J. Yu and Y. Xu, *Catalysts*, 2021, **11**, 991.
6 S. Z. Butler, S. M. Hollen, L. Cao, Y. Cui, J. A. Gupta, H. R. Gutiérrez, T. F. Heinz, S. S. Hong, J. Huang, A. F. Ismach, *et al.*, *ACS Nano*, 2013, **7**, 2898–2926.
7 K. Obodo, G. Gebreyesus, C. Ouma, J. Obodo, S. Ezeonu, D. Rai and B. Bouhafs, *RSC Adv.*, 2020, **10**, 15670–15676.
8 M. Mohl, A.-R. Rautio, G. A. Asres, M. Wasala, P. D. Patil, S. Talapatra and K. Kordas, *Adv. Mater. Interfaces*, 2020, **7**, 2000002.
9 K. Obodo, C. Ouma, J. Obodo, G. Gebreyesus, D. Rai, A. Ukpong and B. Bouhafs, *Nanotechnology*, 2021, **32**, 355502.
10 I. C. Onyia, S. O. Ezeonu, D. Bessarabov and K. O. Obodo, *Comput. Mater. Sci.*, 2021, **197**, 110613.
11 K. O. Obodo, N. Chetty and J. Obodo, *Comput. Mater. Sci.*, 2017, **128**, 373–378.
12 A. K. Sibhatu, G. A. Asres, A. Yimam and T. Teshome, *RSC Adv.*, 2022, **12**, 21270–21279.
13 K. O. Obodo, C. N. M. Ouma, J. T. Obodo and M. Braun, *Phys. Chem. Chem. Phys.*, 2017, **19**, 19050–19057.
14 K. O. Obodo, C. N. Ouma, G. Gebreyesus, J. T. Obodo, S. O. Ezeonu and B. Bouhafs, *Mater. Res. Express*, 2019, **6**, 106307.

15 E. Singh, K. S. Kim, G. Y. Yeom and H. S. Nalwa, *RSC Adv.*, 2017, **7**, 28234–28290.
16 F. Li, W. Wei, P. Zhao, B. Huang and Y. Dai, *J. Phys. Chem. Lett.*, 2017, **8**, 5959–5965.
17 K. O. Obodo, C. N. M. Ouma, J. T. Obodo, M. Braun and D. Bessarabov, *Comput. Condens. Matter*, 2019, **21**, e00419.
18 Y. Yang, Y. Zhang, H. Ye, Z. Yu, Y. Liu, B. Su and W. Xu, *Superlattices Microstruct.*, 2019, **131**, 8–14.
19 D. Muoi, N. N. Hieu, H. T. Phung, H. V. Phuc, B. Amin, B. D. Hoi, N. V. Hieu, L. C. Nhan, C. V. Nguyen and P. Le, *Chem. Phys.*, 2019, **519**, 69–73.
20 K. O. Obodo, C. N. Ouma, G. Gebreyesus, J. T. Obodo and M. Braun, *2018 Open Innovations Conference, OI*, 2018, pp. 115–119.
21 Q. Cheng, J. Pang, D. Sun, J. Wang, S. Zhang, F. Liu, Y. Chen, R. Yang, N. Liang, X. Lu, *et al.*, *InfoMat*, 2020, **2**, 656–697.
22 H. Li, G. Lu, Y. Wang, Z. Yin, C. Cong, Q. He, L. Wang, F. Ding, T. Yu and H. Zhang, *Small*, 2013, **9**, 1974–1981.
23 H. Zeng, G.-B. Liu, J. Dai, Y. Yan, B. Zhu, R. He, L. Xie, S. Xu, X. Chen, W. Yao, *et al.*, *Sci. Rep.*, 2013, **3**, 1–5.
24 R. Tenne and A. Wold, *Appl. Phys. Lett.*, 1985, **47**, 707–709.
25 G. Kakavelakis, A. E. Del Rio Castillo, V. Pellegrini, A. Ansaldo, P. Tzourmpakis, R. Brescia, M. Prato, E. Stratakis, E. Kymakis and F. Bonaccorso, *ACS Nano*, 2017, **11**, 3517–3531.
26 H. Li, J. Wu, Z. Yin and H. Zhang, *Acc. Chem. Res.*, 2014, **47**, 1067–1075.
27 S. Ahn, G. Kim, P. K. Nayak, S. I. Yoon, H. Lim, H.-J. Shin and H. S. Shin, *ACS Nano*, 2016, **10**, 8973–8979.
28 I. C. Gerber and X. Marie, *Phys. Rev. B*, 2018, **98**, 245126.
29 N. Liu, X. D. Weiss and H.-C. Cheng, *Nat. Rev. Mater.*, 2016, **1**(9), 1–17.
30 S. Yu, W. Wei, F. Li, B. Huang and Y. Dai, *Phys. Chem. Chem. Phys.*, 2020, **22**, 25675–25684.
31 M. Yagmurcukardes, Y. Qin, S. Ozen, M. Sayyad, F. M. Peeters, S. Tongay and H. Sahin, *Appl. Phys. Lett.*, 2020, **7**, 011311.
32 L. Cao, Y. S. Ang, Q. Wu and L. Ang, *Appl. Phys. Lett.*, 2019, **115**, 241601.
33 S. Li, M. Shi, J. Yu, S. Li, S. Lei, L. Lin and J. Wang, *Chin. Chem. Lett.*, 2021, **32**, 1977–1982.
34 J. Wang, H. Shu, T. Zhao, P. Liang, N. Wang, D. Cao and X. Chen, *Phys. Chem. Chem. Phys.*, 2018, **20**, 18571–18578.
35 L. Dong, J. Lou and V. B. Shenoy, *ACS Nano*, 2017, **11**, 8242–8248.
36 R. K. Defo, S. Fang, S. N. Shirodkar, G. A. Tritsaris, A. Dimoulas and E. Kaxiras, *Phys. Rev. B*, 2016, **94**, 155310.
37 T. Hu, F. Jia, G. Zhao, J. Wu, A. Stroppa and W. Ren, *Phys. Rev. B*, 2018, **97**, 235404.
38 H. Xiong, J. Sobota, S.-L. Yang, H. Soifer, A. Gauthier, M.-H. Lu, Y.-Y. Lv, S.-H. Yao, D. Lu, M. Hashimoto, *et al.*, *Phys. Rev. B*, 2017, **95**, 195119.
39 K. Zhang, J. K. Kim, B. Park, S. Qian, B. Jin, X. Sheng, H. Zeng, H. Shin, S. H. Oh, C.-L. Lee, *et al.*, *Nano Lett.*, 2017, **17**, 6676–6683.
40 X. Li, Y. Dai, M. Li, W. Wei and B. Huang, *J. Mater. Chem. A*, 2015, **3**, 24055–24063.
41 X. Ma, X. Wu, H. Wang and Y. Wang, *J. Mater. Chem. A*, 2018, **6**, 2295–2301.
42 M. Idrees, H. Din, R. Ali, G. Rehman, T. Hussain, C. Nguyen, I. Ahmad and B. Amin, *Phys. Chem. Chem. Phys.*, 2019, **21**, 18612–18621.
43 Y. Cai, G. Zhang and Y.-W. Zhang, *J. Am. Chem. Soc.*, 2014, **136**, 6269–6275.
44 Y. Zhao, J. Qiao, Z. Yu, P. Yu, K. Xu, S. P. Lau, W. Zhou, Z. Liu, X. Wang, W. Ji, *et al.*, *Adv. Mater.*, 2017, **29**, 1604230.
45 A.-Y. Lu, H. Zhu, J. Xiao, C.-P. Chuu, Y. Han, M.-H. Chiu, C.-C. Cheng, C.-W. Yang, K.-H. Wei, Y. Yang, *et al.*, *Nat. Nanotechnol.*, 2017, **12**, 744–749.
46 J. Li, Z. Huang, W. Ke, J. Yu, K. Ren and Z. Dong, *J. Alloys Compd.*, 2021, **866**, 158774.
47 K. Ren, Y. Luo, S. Wang, J.-P. Chou, J. Yu, W. Tang and M. Sun, *ACS Omega*, 2019, **4**, 21689–21697.
48 K. Ren, J. Yu and W. Tang, *J. Alloys Compd.*, 2020, **812**, 152049.
49 K. Ren, J. Yu and W. Tang, *J. Appl. Phys.*, 2019, **126**, 065701.
50 C.-H. Lee, G.-H. Lee, A. M. Van Der Zande, W. Chen, Y. Li, M. Han, X. Cui, G. Arefe, C. Nuckolls, T. F. Heinz, *et al.*, *Nat. Nanotechnol.*, 2014, **9**, 676–681.
51 R. Meng, J. Jiang, Q. Liang, Q. Yang, C. Tan, X. Sun and X. Chen, *Sci. China Mater.*, 2016, **59**, 1027–1036.
52 T. Roy, M. Tosun, J. S. Kang, A. B. Sachid, S. B. Desai, M. Hettick, C. C. Hu and A. Javey, *ACS Nano*, 2014, **8**, 6259–6264.
53 M.-Y. Li, C.-H. Chen, Y. Shi and L.-J. Li, *Mater. Today*, 2016, **19**, 322–335.
54 P. Giannozzi, S. Baroni, N. Bonini, M. Calandra, R. Car, C. Cavazzoni, D. Ceresoli, G. L. Chiarotti, M. Cococcioni, I. Dabo, *et al.*, *J. Phys.: Condens. Matter*, 2009, **21**, 395502.
55 J. P. Perdew, K. Burke and M. Ernzerhof, *Phys. Rev. Lett.*, 1996, **77**, 3865.
56 X. Zheng, Y. Wei, K. Pang, N. Kaner Tolbert, D. Kong, X. Xu, J. Yang, X. Li and W. Li, *Sci. Rep.*, 2020, **10**, 1–9.
57 J. Heyd, G. E. Scuseria and M. Ernzerhof, *J. Chem. Phys.*, 2003, **118**, 8207–8215.
58 Y. Luo, K. Ren, S. Wang, J.-P. Chou, J. Yu, Z. Sun and M. Sun, *J. Phys. Chem. C*, 2019, **123**, 22742–22751.
59 B. Ghosh, S. Nahas, S. Bhowmick and A. Agarwal, *Phys. Rev. B*, 2015, **91**, 115433.
60 B.-J. Wang, X.-H. Li, R. Zhao, X.-L. Cai, W.-Y. Yu, W.-B. Li, Z.-S. Liu, L.-W. Zhang and S.-H. Ke, *J. Mater. Chem. A*, 2018, **6**, 8923–8929.
61 M. Idrees, H. Din, S. U. Rehman, M. Shafiq, Y. Saeed, H. Bui, C. V. Nguyen and B. Amin, *Phys. Chem. Chem. Phys.*, 2020, **22**, 10351–10359.
62 J. Lou, K. Ren, Z. Huang, W. Huo, Z. Zhu and J. Yu, *RSC Adv.*, 2021, **11**, 29576–29584.
63 A. Rawat, M. K. Mohanta, N. Jena, Dimple, R. Ahammed and A. De Sarkar, *J. Phys. Chem. C*, 2020, **124**, 10385–10397.
64 L. Cao, Y. Deng, H. Gao, Y. Wang, X. Chen and Z. Zhu, *Phys. Chem. Chem. Phys.*, 2015, **17**, 6809–6818.
65 K. O. Obodo, C. N. M. Ouma, P. M. Modisha and D. Bessarabov, *Appl. Surf. Sci.*, 2020, **529**, 147186.

66 S. Wang, C. Ren, H. Tian, J. Yu and M. Sun, *Phys. Chem. Chem. Phys.*, 2018, **20**, 13394–13399.
67 Y. Zhang, R. Xiong, B. Sa, J. Zhou and Z. Sun, *Sustainable Energy Fuels*, 2021, **5**, 135–143.
68 M. R. Filip, C. Verdi and F. Giustino, *J. Phys. Chem. C*, 2015, **119**, 25209–25219.
69 H. J. Snaith, *Adv. Funct. Mater.*, 2010, **20**, 13–19.
70 W. Shockley and H. J. Queisser, *J. Appl. Phys.*, 1961, **32**, 510–519.
71 S. K. Pradhan, B. Xiao and A. K. Pradhan, *Sol. Energy Mater. Sol. Cells*, 2016, **144**, 117–127.
72 Z. Ma, R. Li, R. Xiong, Y. Zhang, C. Xu, C. Wen and B. Sa, *Materials*, 2021, **14**, 3768.
73 P. Lin and J. Yang, *J. Alloys Compd.*, 2020, **842**, 155890.
74 J. Chen, X. He, B. Sa, J. Zhou, C. Xu, C. Wen and Z. Sun, *Nanoscale*, 2019, **11**, 6431–6444.
75 K. Maeda and K. Domen, *J. Phys. Chem. Lett.*, 2010, **1**, 2655–2661.
76 K. Maeda, *J. Photochem. Photobiol., C*, 2011, **12**, 237–268.
77 L. Shi, B. Yan, D. Shao, F. Jiang, D. Wang and A. Lu, *Catal*, 2017, **38**, 389–395.
78 B. Y. Alfaifi, H. Ullah, S. Alfaifi, A. A. Tahir and T. K. Mallick, *Veruscript Funct. Nanomater.*, 2018, **2**, BDJOC3.
79 J. Wang, X. Yang, J. Cao, Y. Wang and Q. Li, *Comput. Mater. Sci.*, 2018, **150**, 432–438.
80 T. Shinagawa and K. Takanabe, *ChemSusChem*, 2017, **10**, 1318–1336.